Imperfect photon detection in quantum illumination

F. Kronowetter,[1,2,3,*,‡] M. Würth,[4,‡] W. Utschick,[4] R. Gross,[1,2,5] and K.G. Fedorov[1,2,5,†]

[1] *Walther-Meißner-Institut, Bayerische Akademie der Wissenschaften, Garching 85748, Germany*

[2] *TUM School of Natural Sciences, Physics Department, Technical University of Munich, Garching 85748, Germany*

[3] *Rohde & Schwarz GmbH & Co. KG, Mühldorfstraße 15, Munich 81671, Germany*

[4] *Technical University of Munich, TUM School of Computation, Information and Technology, Munich 80290, Germany*

[5] *Munich Center for Quantum Science and Technology (MCQST), Munich 80799, Germany*

(Received 8 August 2023; accepted 22 December 2023; published 5 January 2024)

In quantum illumination, various detection schemes have been proposed for harnessing the remaining quantum correlations of the entanglement-based resource state. To date, the only successful implementation in the microwave domain [R. Assouly, R. Dassonneville, T. Peronnin, A. Bienfait, and B. Huard, Nat. Phys. **19**, 1418 (2023)] has relied on a specific mixing operation of the respective return and idler modes, followed by single-photon counting in one of the two mixer outputs. We investigate the performance of this scheme for realistic detection parameters in terms of the detection efficiency, dark-count probability, and photon-number resolution. Furthermore, we take the second mixer output into account and investigate the advantage of correlated photon counting (CPC) for a varying thermal background and optimum postprocessing weighting in CPC. We find that the requirements for photon-number resolution in the two mixer outputs are highly asymmetric due to different associated photon-number expectation values.

DOI: 10.1103/PhysRevApplied.21.014007

I. INTRODUCTION

Nonclassical correlations in propagating signals provide the essential ingredient for quantum illumination (QI) [1,2]. In QI, a general application scenario is the presence detection of a low-reflectivity object embedded in a bright thermal background. For that purpose, one mode of the entangled resource state is sent as a probe signal, while the other mode is preserved for further use in a joint detection step [2]. Most importantly, QI is robust against entanglement-breaking background noise, which results in an enhanced performance compared to the ideal classical reference scheme based on coherent-state transmission. Propagating two-mode squeezed vacuum states represent an ideal resource for QI and can be routinely generated with various superconducting parametric circuits [3–6]. An optimal detector layout remains an open question, because the full 6-dB quantum advantage (QA) in the error exponent requires very cumbersome and demanding experimental setups [7,8]. However, a 3-dB quantum advantage over the ideal classical radar can be achieved by using more practically accessible schemes. Among those are the parametric mixer (PM) and phase-conjugate receivers, both of which rely on single-photon detection or counting as a final step [9]. Up to the present time, the only experimental implementation of a microwave quantum radar achieving a genuine quantum advantage relies on the PM-type receiver [10].

In this work, we focus on the PM scheme [cf. Fig. 1(a)] in the asymptotic regime with realistic microwave-photon-detector properties. We start with an ideal scenario of perfect photon counters (PCs). Next, we analyze the PM-receiver performance with nonunity detection efficiencies, nonzero dark-count probabilities, and finite photon-number resolution [cf. Fig. 1(b)]. Furthermore, we consider a scheme with two independent PCs and compare its performance with a postprocessing protocol, which takes into account the correlated-photon-counting (CPC) results of both PCs [11]. We find that the respective expectation values of the two photon-number operators are highly asymmetric. This is due to the fact that the photon-number expectation value at PC1 is governed by the number of signal photons per mode, $N_S \ll 1$, while the photon number at PC2 is dictated by the number of thermal background photons, $N_B \gg 1$. As a consequence, PC1 does not require a photon-number resolution, $K > 1$, even for a thermal background of 1000 photons. Conversely,

*fabian.kronowetter@wmi.badw.de

†kirill.fedorov@wmi.badw.de

‡These authors contributed equally to this work.

PC2 does not outperform the ideal classical radar in individual detection, even with infinite photon-number resolution, $K \to \infty$. Furthermore, we find that the receiver based on CPC performs better than PC1 alone. This performance enhancement is due to the highly correlated nature of the detector (PC1 and PC2) outputs. Independent photon counting shows a similar sensitivity toward finite detection efficiencies as the CPC approaches. We investigate a weighting of the individual PC measurement results as a function of the system parameters for CPC and identify an optimum balance between the PCs.

II. QUANTUM ILLUMINATION PROTOCOL

The QI scheme relies on quantum-enhanced remote sensing by exploiting quantum correlations between M spatially separated pairs of signal and idler modes, described by the bosonic operators $\hat{a}_S$ and $\hat{a}_I$, respectively. These quantum correlations are encoded in pure entangled zero-mean Gaussian states that are fully characterized by the corresponding covariance matrix

$$\mathbf{V}_{SI} = \langle [\hat{a}_S\, \hat{a}_I\, \hat{a}_S^\dagger\, \hat{a}_I^\dagger]^T [\hat{a}_S^\dagger\, \hat{a}_I^\dagger\, \hat{a}_S\, \hat{a}_I] \rangle \tag{1}$$

$$= \begin{bmatrix} (N_S+1)\,\mathbb{I}_2 & C_q\,\boldsymbol{\sigma}_X \\ C_q\,\boldsymbol{\sigma}_X & N_S\,\mathbb{I}_2 \end{bmatrix}, \tag{2}$$

where N_S is the mean photon number of the respective signal and idler modes, $\mathbb{I}_2$ is the two-dimensional identity matrix, the quantity $C_q = \sqrt{N_S(N_S+1)}$ encodes the strength of the quantum correlations, and $\boldsymbol{\sigma}_X$ is the Pauli-X matrix. In this framework, the signal mode interrogates a region of interest, while the idler mode is retained and stored for a round-trip time of the signal. For the task of a binary decision between hypothesis H_0 (target absent) and hypothesis H_1 (target present), the return modes entering the receiving unit are given by

$$\hat{a}_R|_{H_0} = \hat{a}_B, \tag{3}$$

$$\hat{a}_R|_{H_1} = e^{i\theta}\sqrt{\kappa}\,\hat{a}_S + \sqrt{1-\kappa}\,\hat{a}_B, \tag{4}$$

where $\hat{a}_B$ represents a thermal state with mean photon number $N_B = \langle \hat{a}_B^\dagger \hat{a}_B \rangle \gg 1$, θ is an overall phase shift, and $\kappa \ll 1$ is the round-trip signal loss. Note that under H_1, $N_B/(1-\kappa)$ thermal photons are encoded in $\hat{a}_B$ for equal background photon numbers under both hypotheses [9]. Since we focus on QI and do not consider quantum phase estimation, we set $\theta = 0$ [8]. The resulting joint return-idler state is again characterized by zero-mean Gaussian states with

$$\mathbf{V}_{RI} = \langle [\hat{a}_R\, \hat{a}_I\, \hat{a}_R^\dagger\, \hat{a}_I^\dagger]^T [\hat{a}_R^\dagger\, \hat{a}_I^\dagger\, \hat{a}_R\, \hat{a}_I] \rangle \tag{5}$$

$$\overset{H_0}{=} \begin{bmatrix} N_B+1 & 0 & 0 & 0 \\ 0 & N_S+1 & 0 & 0 \\ 0 & 0 & N_B & 0 \\ 0 & 0 & 0 & N_S \end{bmatrix} \tag{6}$$

$$\overset{H_1}{=} \begin{bmatrix} \kappa N_S + N_B + 1 & 0 & 0 & \sqrt{\kappa} C_q \\ 0 & N_S+1 & \sqrt{\kappa} C_q & 0 \\ 0 & \sqrt{\kappa} C_q & \kappa N_S + N_B & 0 \\ \sqrt{\kappa} C_q & 0 & 0 & N_S \end{bmatrix}. \tag{7}$$

The minimum error probability, $P_{e,\min}$, for this binary decision task is upper bounded by the quantum Chernoff bound (QCB), $P_{e,\min} \le 0.5 \exp(-R_Q M)$, which is asymptotically tight for $M \to \infty$ and connected to the error exponent R_Q. A typical classical reference scheme is a coherent-state (CS) transmitter with a mean photon number N_S per mode, which achieves an error exponent $R_C = \kappa N_S/(4N_B)$. In the weak-transmission ($N_S \ll 1$), bright-background ($N_B \gg 1$), and high-loss ($\kappa \ll 1$) limit, the QI protocol has an error exponent $R_Q = \kappa N_S/N_B$ that is 6 dB larger than R_C [2].

The goal of various proposed receiver schemes is to reach this theoretical 6-dB QA. From Eqs. (6) and (7), it is obvious that the potential of the entanglement-assisted protocol does not stem from local properties of the individual modes (i.e., the diagonal $\mathbf{V}_{RI}$ entries) but, rather, from the remaining nonlocal correlations (i.e., the antidiagonal $\mathbf{V}_{RI}$ entries) characterized by $\langle \hat{a}_R \hat{a}_S \rangle = \langle \hat{a}_R^\dagger \hat{a}_S^\dagger \rangle = \sqrt{\kappa} C_q$ with $\left[\hat{a}_R, \hat{a}_S\right] = \left[\hat{a}_R^\dagger, \hat{a}_S^\dagger\right] = 0$. This fundamental result leads to the intuition that a joint measurement of $\hat{a}_R$ and $\hat{a}_I$ is a prerequisite for achieving the QA [2,9,11]. A potential workaround for this joint measurement might be implemented with a feed-forward heterodyne scheme, which also avoids using single-photon detectors (SPDs) or counters [12]. Moreover, a variant of this scheme exploiting reprogrammable beam splitters promises the full 6-dB QA [8]. However, its experimental implementation remains very challenging in the microwave regime, due to the absence of required components.

The QI paradigm is closely related to quantum parameter estimation, e.g., for estimating the reflectivity κ of the object [13]. In the realm of quantum parameter estimation, the quantum Fisher information (QFI) represents the central figure of merit and is connected to the Cramér-Rao bound, which gives an upper limit for the obtainable precision of the unbiased estimator $\hat{\kappa}$,

$$\Delta\hat{\kappa}^2 \ge \frac{1}{M\mathcal{F}}, \tag{8}$$

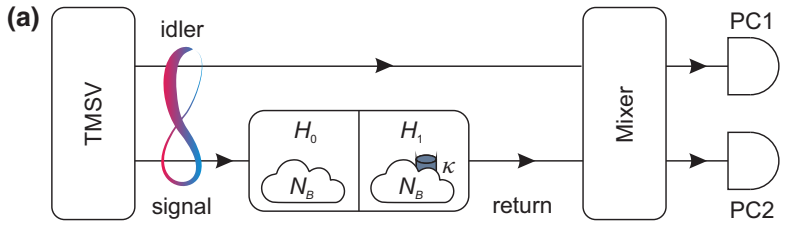

(b)

Detector parameters		
	PC1	PC2
Efficiency η	η_1	η_2
Dark-count probability P_{dc}	$P_{dc,1}$	$P_{dc,2}$
Resolution K	K_1	K_2

FIG. 1. (a) An illustration of the considered quantum illumination scheme. One mode of a two-mode squeezed vacuum state (TMSV), characterized by N_S photons per entangled mode, serves as a signal source. While the idler mode can directly pass to the PM receiver, the signal propagates through a bright thermal background characterized by the number of noise photons, N_B. Under the hypothesis H_0 (no target present), the entire signal is lost and only N_B thermal photons enter the receiver via the signal path. Under H_1 (target present), the signal is weakly reflected from the target (with reflectivity $\kappa \ll 1$) and $N_B + \kappa N_S$ photons enter the receiver via the signal path. The receiver consists of a mixer, implementing an interaction between the retained idler and return signal modes, followed by two single-photon counters, PC1 and PC2. (b) The PCs can be characterized by their detection efficiency, η, dark-count probability, P_{dc}, and photon-number resolution, K. We analyze the performance of the overall scheme in terms of error probabilities for realistic values of η, P_{dc}, and K in order to test the robustness of the QI quantum advantage in presently accessible experimental settings.

where $\mathcal{F}$ denotes the QFI. In the framework of QI, the enhancement of the QFI with respect to the optimal classical case is limited to 3 dB, i.e., $\mathcal{F}_{QI}/\mathcal{F}_C \leq 2$, where $\mathcal{F}_{QI}$ denotes the QFI associated with the QI protocol and $\mathcal{F}_C$ represents the classical counterpart [13]. For Gaussian QI, the QFI can be expressed as [13]

$$\mathcal{F}_{QI} = \frac{4N_S}{(N_B+1)\left(1+\frac{N_S}{N_S+1}\frac{N_B}{N_B+1}\right)}. \tag{9}$$

In principle, the QI task can be mapped onto quantum parameter estimation via a corresponding error probability [13,14]

$$P_e \sim \exp(-\kappa^2 \mathcal{F}_{QI} M/8), \tag{10}$$

which is valid for pairwise joint measurements, as realized in the PM-type receiver (cf. Sec. III A). For large M, Eq. (10) converges toward the 3-dB QA for $N_S \ll 1$, $N_B \gg 1$, and $\kappa \ll 1$, in accordance with the QI theory for this class of receiver [9,11]. In this work, we are interested in the binary target-detection problem, as opposed to the continuous-valued parameter estimation. Accordingly, we use the QCB for the performance evaluation of various receiver schemes. Nonetheless, Eq. (10) provides a useful general illustration on the connection between the QFI and the QCB.

III. RESULTS AND DISCUSSION

A. Ideal PM-receiver characteristics

As of the present time, the only successful experimental implementation of a microwave quantum radar has relied on the PM-type receiver, schematically shown in Fig. 1(a) [10]. In this approach, the return and idler modes interact nonlinearly, forming the input-output relations

$$\hat{b}_1 = \sqrt{G}\,\hat{a}_I + \sqrt{G-1}\,\hat{a}_R^\dagger, \tag{11}$$

$$\hat{b}_2 = \sqrt{G}\,\hat{a}_R + \sqrt{G-1}\,\hat{a}_I^\dagger, \tag{12}$$

where $G = 1+\varepsilon^2$ is the mixer gain and $\varepsilon \ll 1$. Originally, it was proposed to use an optical parametric amplifier for implementing this input-output relation [9]. In the microwave domain, a Josephson ring modulator or a degenerate Josephson mixer realize the same transformation [10,15,16]. The optimal mixer gain, G^*, has been derived in Ref. [8] as a function of the system parameters, N_S, N_B, and κ. The mixer is followed by single-photon counters, PC1 and PC2, with

$$N_1 = \langle \hat{b}_1^\dagger \hat{b}_1 \rangle = G\langle \hat{a}_I^\dagger \hat{a}_I \rangle + \sqrt{G(G-1)}\left(\langle \hat{a}_R^\dagger \hat{a}_I^\dagger \rangle + \langle \hat{a}_R \hat{a}_I \rangle\right) + (G-1)\,\langle \hat{a}_R \hat{a}_R^\dagger \rangle \tag{13}$$

and

$$N_2 = \langle \hat{b}_2^\dagger \hat{b}_2 \rangle = G\langle \hat{a}_R^\dagger \hat{a}_R \rangle + \sqrt{G(G-1)}\left(\langle \hat{a}_R^\dagger \hat{a}_I^\dagger \rangle + \langle \hat{a}_R \hat{a}_I \rangle\right) + (G-1)\,\langle \hat{a}_I \hat{a}_I^\dagger \rangle, \tag{14}$$

as the respective photon numbers. As can be seen from Eqs. (6) and (7), the return mode $\hat{a}_R$ is characterized by $\langle \hat{a}_R^\dagger \hat{a}_R \rangle = N_B$ under H_0 and $\langle \hat{a}_R^\dagger \hat{a}_R \rangle = N_B + \kappa N_S$ under H_1. The nonlocal correlations, $\langle \hat{a}_R^\dagger \hat{a}_I^\dagger \rangle = \langle \hat{a}_R \hat{a}_I \rangle = 0$, vanish for H_0 and are given by $\langle \hat{a}_R^\dagger \hat{a}_I^\dagger \rangle = \langle \hat{a}_R \hat{a}_I \rangle = \sqrt{\kappa} C_q$ for H_1.

All detection protocols perform a maximum-likelihood analysis of the photon-number statistics, which is based on photon counting through M return-idler transmitted modes. Irrespective of the detection scheme (individual or CPC), it is assumed that for both hypotheses the conditional distributions converge to a normal distribution for

$M \gg 1$ according to the central limit theorem. The decision threshold for the maximum-likelihood test is given by [17]

$$N_{\text{th}} = M \frac{\sigma|_{H_1}\,\mu|_{H_0} + \sigma|_{H_0}\,\mu|_{H_1}}{\sigma|_{H_0} + \sigma|_{H_1}}, \tag{15}$$

where $\mu|_{H_{0,1}}$ and $\sigma^2|_{H_{0,1}}$ are the mean and variance of the photon-number distribution under the two hypotheses, respectively. The obtained overlap of the two distributions defines the error probability of the scheme. This overlap depends on the difference of the means $\Delta\mu_i = |N_i|_{H_1} - N_i|_{H_0}|$ $(i = 1, 2)$, as well as on the respective variances $\sigma_i^2|_{H_{0,1}} = N_i(N_i + 1)|_{H_{0,1}}$, where both quantities scale linearly with the total number of transmitted modes [9]. Since $N_1|_{H_{0,1}} \ll 1$, it follows that $\sigma_1^2|_{H_{0,1}} \approx N_1 \ll 1$, which results in a small overlap of the two distributions and a low resulting error probability (cf. Fig. 2). Conversely, for the same parameters, $N_2 \approx 20.104|_{H_0}$ $(N_2 \approx 20.105|_{H_1})$ is dominated by $G\langle\hat{a}_R^\dagger\hat{a}_R\rangle \approx N_B$ and yields photon-number distributions with variances $\sigma_2^2|_{H_{0,1}} \approx N_2^2 \gg 1 \gg \sigma_1^2|_{H_{0,1}}$, while $\Delta N_2 \approx \Delta N_1$. The associated error probability of N_2 is much larger than that of N_1 and clearly inferior to the ideal classical reference scheme, as shown in Fig. 2. Note that the considered maximum-likelihood test yields the minimum possible error probability in a scenario where the prior distribution of the two hypotheses is unknown and is thus optimal [18]. To conclude, the PM-type receiver shows a strong asymmetry of the detection performance in individual detection, where only PC1 (in our convention) shows a QA.

B. (Un)balanced difference detection

Las Heras *et al.* [11] have considered the PM-type receiver exploiting both PCs by analyzing the operator $\hat{O} = G\hat{N}_1 - (G-1)\,\hat{N}_2$. Note that this difference detector (CPC in our convention) is unbalanced with weights G and $G - 1$, such that the decisive nonlocal correlations persist in $\hat{O}$ [cf. Eqs. (13) and (14)]. The PCR scheme also utilizes the measurement outcome of both single-photon counters in a balanced difference detector with $\hat{N} = \hat{N}_1 - \hat{N}_2$ [9]. In the following, we compare the performance of the PM-type scheme in individual photon counting with the CPC approach, which implements the operator $\hat{O}$ (see Fig. 3). The benefit of the CPC with respect to individual detection (PC1) is similar for $N_B = 20$ [Fig. 3(a)] and $N_B = 1000$ [Fig. 3(b)]. Note that for $\log_{10}(M) < 7$ in Fig. 3(b), the QCB lies above the performances of CPC and PC1 and can only be interpreted as an upper bound to the associated error probabilities [2,9]. Similarly, we observe a second crossing of the QCB and the CS reference at an even lower $\log_{10}(M) \approx 6.5$. These features can be explained by the QCB reaching the asymptotic regime only when $M \gg N_B/(\kappa N_S)$, corresponding to the error probability converging toward zero, which occurs for $M \gg 10^7$ in Fig. 3(b) [2]. For Fig. 3(a), this criterion yields $M \gg 2 \times 10^5$ and is fulfilled for the entire range of M. Large correlations between individual photon-counting events of PC1 and PC2, illustrated by Eqs. (19) and (20), result in the enhanced performance of the CPC. The operator $\hat{O}$ can be more generally described as

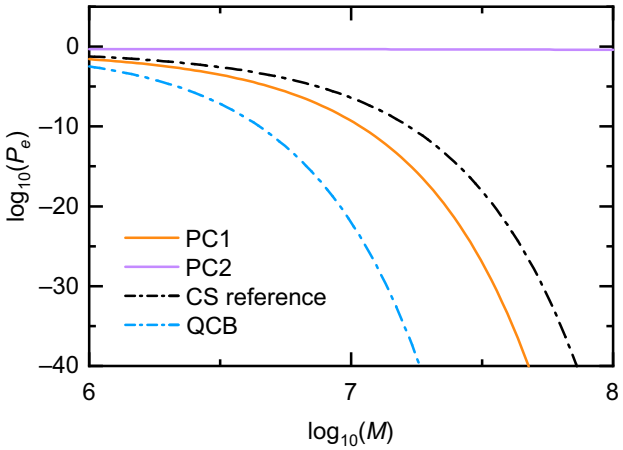

FIG. 2. The error probability P_e as a function of the number of transmitted modes M for individual single-photon counting with PC1 (orange) and PC2 (purple) in an PM-type QI scheme. The dot-dashed black line represents the error probability of the ideal classical reference radar (a CS transmitter with a coherent photon number N_S in combination with a homodyne detector), which coincides with the Helstrom (lower) bound for classical state transmitters [17]. The dot-dashed blue line depicts the quantum Chernoff (upper) bound for entanglement-based QI schemes. The employed system parameters are $N_S = 0.01$, $N_B = 20$, $\kappa = 0.01$, and $G = G^*$.

$$\hat{O} = w_1\hat{N}_1 - w_2\hat{N}_2, \tag{16}$$

where w_1 and w_2 are the weights of the measured photon numbers in postprocessing, such that they are not constricted by the experimental conditions. The expectation value and variance of $\hat{O}$ are given by

$$\langle\hat{O}\rangle = w_1\langle\hat{N}_1\rangle - w_2\langle\hat{N}_2\rangle \tag{17}$$

and

$$\begin{aligned}\text{Var}\left(\hat{O}\right) = w_1^2\,\text{Var}\left(\hat{N}_1\right) + w_2^2\,\text{Var}\left(\hat{N}_2\right) \\ - 2w_1w_2\text{Cov}\left(\hat{N}_1, \hat{N}_2\right),\end{aligned} \tag{18}$$

where $\text{Var}(\hat{N}_i) = N_i\,(N_i + 1)$ for $i = 1, 2$. Under the hypotheses H_0 and H_1, the corresponding covariances

yield

$$\mathrm{Cov}\left(\hat{N}_1,\hat{N}_2\right)\Big|_{H_0} = G\,(G-1)\;(N_S+N_B+1)^2\,, \quad (19)$$

$$\mathrm{Cov}\left(\hat{N}_1,\hat{N}_2\right)\Big|_{H_1} = \Big((2G-1)\,C_q + +\sqrt{G\,(G-1)} \times (N_S\,(\kappa+1)+N_B+1)\Big)^2, \quad (20)$$

as detailed in the Appendix. Figure 4(a) shows the QA of the CPC approach as a function of w_1 and w_2. Here, the conventional weighting according to Ref. [11], $w_1 = G$ and $w_2 = G-1$ (solid red line), has a large gradient with respect to the optimal working regime (blue), such that a small change or misestimation of G can lead to a complete loss of the QA [white star versus black star; see also Fig. 4(b)]. We identify an optimal weighting according to

$$w_2 = \frac{\sqrt{N_S(N_S+1)(N_B+\kappa N_S)(N_B+\kappa N_S+1)}}{(N_B+(\kappa-1)N_S)(N_B+(\kappa+1)N_S+1)} + \frac{N_S(N_S+1)}{(N_B+(\kappa-1)N_S)(N_B+(\kappa+1)N_S+1)}\,w_1 = (G^*-1)\,w_1, \quad (21)$$

shown as the dashed white line in Fig. 4(a), which relaxes the requirements in terms of parameter precision and introduces a degree of freedom in the choice of the postprocessing weights.

C. Practical PM-receiver characteristics

Realistic quantum illumination implementations may contain detection imperfections [10,19]. Here, we analyze the practical limitations of microwave PCs and their impact on the PM-type receiver. Although single-photon detection for propagating microwaves is challenging due to the low photon energies, which are approximately 5 orders of magnitude smaller than for optical photons, various theoretical concepts [20–30] have paved the way to successful experimental implementations [31–37]. Here, most advanced schemes exploit Ramsey interferometry to implement quantum nondemolition detection, or counting, of incident microwave photons by measuring a photon-induced phase perturbation of an ancilla qubit [33,34]. Since the qubit coherence time directly correlates with the dark-count rate, the performance of Ramsey-based detectors strongly depends on a sufficiently long qubit lifetime. Apart from the dark-count rate and the detection efficiency, the photon-number resolution is another key parameter in single-photon detection. Dassonneville *et al.* [37] have realized a number-resolving photon counter of up to three photons, which we consider in our analysis as a reference (cf. Sec. III C 2). The dead time of SPDs [38] represents a further important quantity, which we do not discuss in detail in this work. Modern microwave detection schemes achieve dead times between 100 ns [33] and several microseconds [37,39].

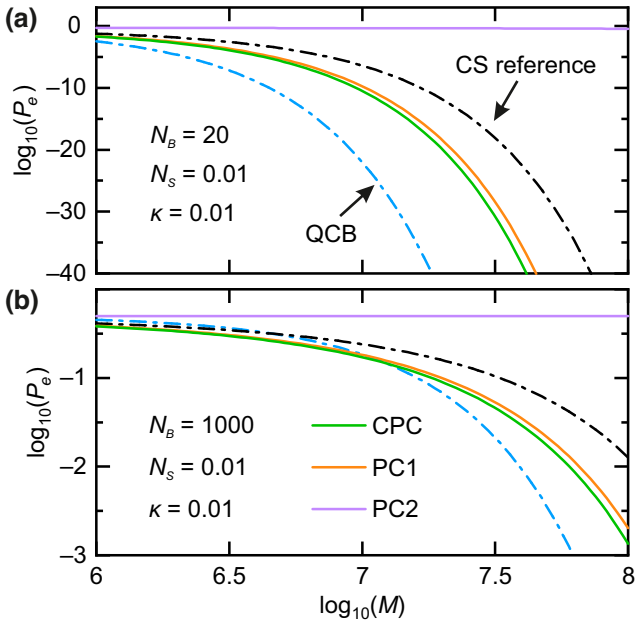

FIG. 3. The error probability P_e as a function of transmitted modes M for individual single-photon detection and CPC with $w_1 = G$ and $w_2 = G-1$ for (a) $N_B = 20$ coupled background photons and (b) $N_B = 1000$. The black dash-dotted line represents the error probability of the ideal CS radar. The blue dash-dotted line depicts the corresponding QCB. The green line depicts the ideal CPC performance, while the orange (purple) line shows the results for individual detection with PC1 (PC2). The employed system parameters are $N_S = 0.01$, $\kappa = 0.01$, and $G = G^*$.

1. Finite detection efficiencies

State-of-the-art microwave SPDs achieve a click probability $P_c = 0.93$ for an incoming single photon with a dark-count probability $P_{\mathrm{dc}} = 0.03$ [37]. The dark-count probability can be computed as the dark-count rate times the duration of the detection window. Moreover, $P_c = 1 - P_{|1\rangle}(0)$, where $P_{|1\rangle}(0)$ is the probability of measuring no click for an impinging single photon. To date, the quality of photon-number-resolved measurements, expressed by the conditional probabilities $P_{|k\rangle}(l)$ of realizing a measurement outcome $l = \{0,\ldots,3\}$ for an incoming Fock state $|k\rangle$ strongly depends on k, with $P_{|1\rangle}(1) = 76\%, P_{|2\rangle}(2) = 71\%$ and $P_{|3\rangle}(3) = 54\%$ [37]. For simplicity, we assume a photon-number resolution corresponding to the SPD click probability, i.e., $P_{|k\rangle}(k) = P_c = 0.93$ for all $k = 1,2,\ldots$, which effectively gives an upper performance bound. We model the influence of finite dark-count probabilities and a finite detection efficiency $P_{|k\rangle}(k) < 1$ with a beam splitter

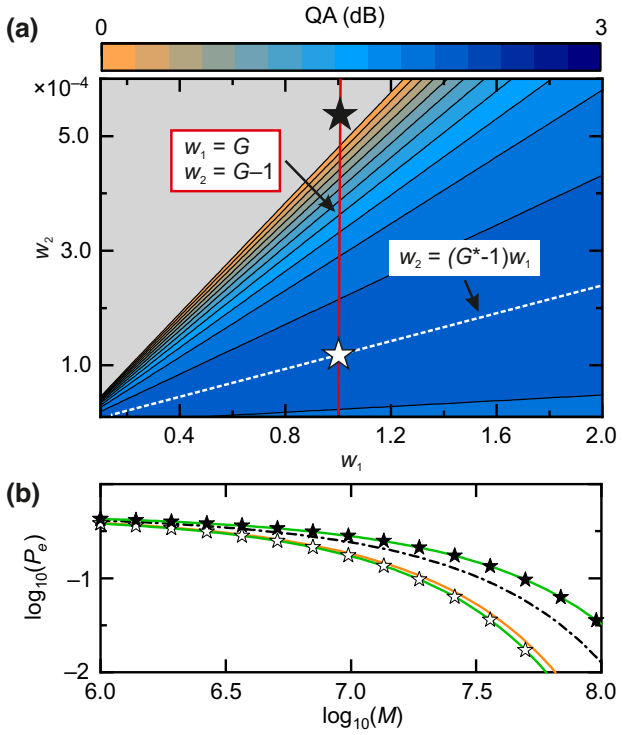

FIG. 4. (a) The QA as a function of the weights w_1 and w_2. The solid red line represents weighting according to $w_1 = G$ and $w_2 = G - 1$ [11]. While this relation (white star) can yield the full 3-dB QA (blue color code), a slight variation or misestimation of G on the order of 0.05% (black star) already leads to inferior results with respect to the CS reference. The dashed white line represents an optimal weighting according to Eq. (21). (b) The resulting error probability as a function of the transmitted modes for the optimal weighting (green line with white stars) versus a misestimated weighting (green line with black stars) in comparison with individual detection (PC1, orange) and the CS reference (dash-dotted black line). The system parameters are $N_S = 0.01, \kappa = 0.01, N_B = 1000$, and $G = G^*$.

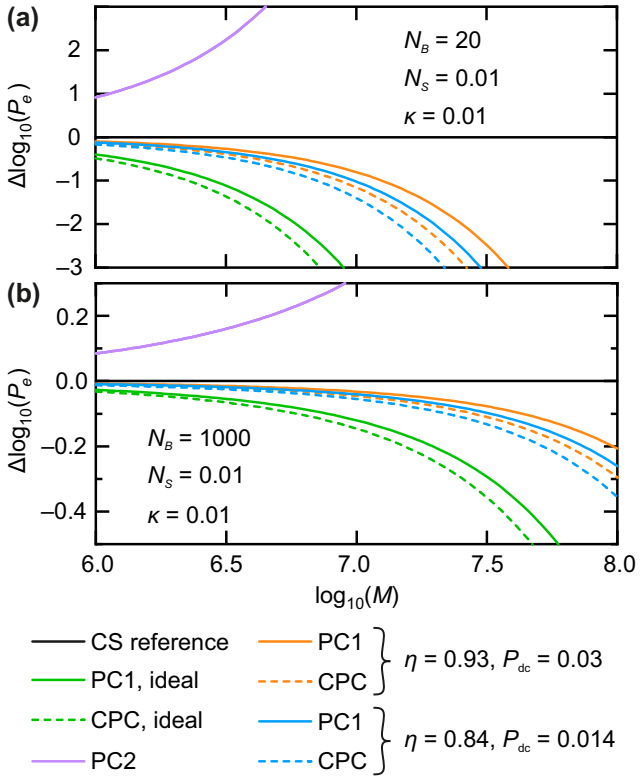

FIG. 5. The error-probability difference $\Delta\log_{10}(P_e) = \log_{10}(P_e) - \log_{10}(P_{e,\mathrm{CS}})$ as a function of the number of transmitted modes M for individual photon counting (solid lines) and optimal [according to Eq. (21)] CPC (dashed lines) for (a) $N_B = 20$ coupled background photons and (b) $N_B = 1000$. The black line represents the error probability of the CS reference. The green lines depict ideal detectors, the orange lines correspond to $\eta = 0.93$ and $P_{\mathrm{dc}} = 0.03$, and the blue lines show the performance for $\eta = 0.84$ and $P_{\mathrm{dc}} = 0.014$. The purple line shows the results for PC2, which are close to $P_e = 0.5$ in each of the three considered cases. The mixer gain is set to $G = G^*$.

before an ideal PC,

$$\hat{c}_i = \sqrt{\eta}\,\hat{b}_i + \sqrt{1-\eta}\,\hat{b}_{c,i}, \tag{22}$$

where $i = 1, 2$, $\eta = P_{|k\rangle}(k)$ is the beam-splitter transmissivity, and the dark-count probability is modeled with a coupled mode $\hat{b}_{c,i} = 1/\sqrt{1-\eta}\,\hat{a}_{\mathrm{th},i}$ characterized by $\langle \hat{a}^\dagger_{\mathrm{th},i}\hat{a}_{\mathrm{th},i}\rangle = (1/(1-P_{\mathrm{dc}}) - 1) \approx P_{\mathrm{dc}}$ for $P_{\mathrm{dc}} \ll 1$. Accordingly, we do not take into account the influence of $P_{|k\rangle}(l)$ for $k \neq l$.

In Fig. 5, we plot the error-probability difference for $N_B = 20$ [Fig. 5(a)] and for $N_B = 1000$ [Fig. 5(b)]. We compare the ideal performance of individual and CPC detection for a given CS reference in two realistic scenarios: high efficiency and moderate dark-count probability [37] versus moderate efficiency and low dark-count probability [34]. For $N_B = 20$, both scenarios yield clearly inferior results compared to the ideal case. We observe that the scenario with a low dark-count probability outperforms the high-efficiency counterpart, which underlines that for a realistic implementation, the minimization of dark-count probabilities plays a decisive role for photon detection in QI. Additionally, the CPC approach only marginally beats individual detection for all three scenarios in the low-noise case of $N_B = 20$. The high-noise regime, $N_B = 1000$, shows similar results, with the low-dark-count detector performing slightly better than the high-efficiency case and a consistent performance enhancement for the CPC. In both noise regimes, PC2 does not exhibit a strong dependence on the nonidealities, since $P_e \approx 0.5$ already in the ideal case.

Figure 6 illustrates the performance of various already demonstrated microwave SPDs, in terms of P_{dc} and η, for achieving a QA in individual detection with PC1. In accordance with the successful microwave quantum radar

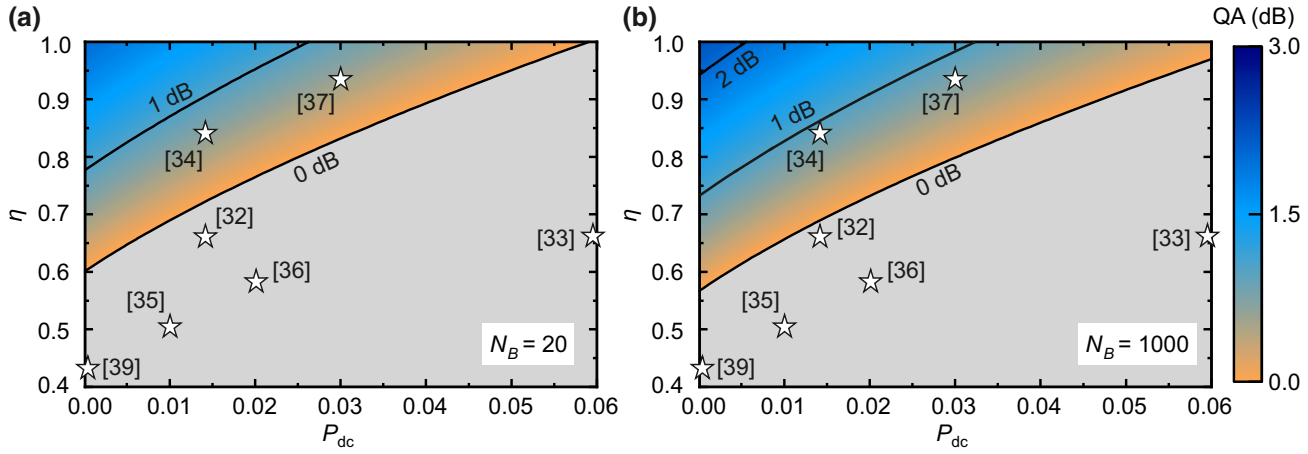

FIG. 6. The QA for individual detection with PC1 as a function of the dark-count probability P_{dc} and the detection efficiency η for (a) $N_B = 20$ and (b) $N_B = 1000$. The white stars indicate the performance of microwave SPD implementations from Refs. [32–37,39]. The gray color code illustrates a region without any QA. The other employed system parameters are $N_S = 0.01$, $\kappa = 0.01$, and $G = G^*$.

realization [10], the underlying device investigated by Dassonneville *et al.* [37] is situated in the region of a robust QA. Importantly, the QA vanishes rapidly with increasing P_{dc}, even for an ideal detection efficiency of $\eta = 1$. Conversely, the scheme is robust against finite efficiencies, $\eta < 1$, down to $\eta \approx 0.6$ for $N_B \gg 1$ [cf. Fig. 6]. These findings suggest that the minimization of P_{dc} in combination with a reasonably high η is desirable in order to achieve the QA, in agreement with our results from Fig. 5. In accordance with theory, the maximally reachable QA increases with increasing N_B, as can also be seen in Figs. 6(a) and 6(b). As a consequence, the area of QA > 0 increases and, e.g., the 1-dB and 0-dB QA lines lean toward lower values of P_{dc} and η. We would like to mention that the mapping of existing SPDs onto the QA problem in Fig. 6 may be limited to various simplifications of our theoretical model and should not be considered as an overall evaluation of the performance of those detectors.

2. Finite detection resolution

In principle, photon counters can provide full access to the photon-number operator in Eqs. (13) and (14). However, existing state-of-the-art microwave single-photon counters exhibit a rather limited photon-number resolution [34,36,37]. To analyze the impact of this finite resolution, we restrict the PCs in Fig. 1 to a resolution up to K photons. Therefore, a single measurement has possible outcomes of measuring $0, 1, \ldots, K$ photons and we assume that the measurement yields K if the number of photons in the probe is larger than or equal to K. Under both hypotheses, the state at the output of the mixer is a thermal state with mean photon number $N_i, i \in \{1, 2\}$, given by Eqs. (13) and (14) [9]. This yields a photon-number distribution at the output of the photon counter,

$$p(n) = \begin{cases} (1-q_i)q_i^n, & 0 \le n < K, \\ 1 - (1-q_i)\sum_{k=0}^{K-1} q_i^k, & n = K, \end{cases} \tag{23}$$

with $q_i = N_i/N_i + 1$. For this distribution, the expectation value is given by

$$\mu_i^{(K)} = \frac{q_i(1-q_i^K)}{1-q_i} \tag{24}$$

and the respective variance can be written as

$$\sigma_i^{2,(K)} = \frac{q_i}{1-q_i}\left(1 - (2K+1)q_i^K + 2q_i\frac{1-q_i^K}{1-q_i}\right) - \left(\frac{q_i(1-q_i^K)}{1-q_i}\right)^2. \tag{25}$$

Analogously to Sec. III A, the assumption of a large number of transmitted modes, i.e., $M \gg 1$, leads to the threshold given in Eq. (15) but with a mean and standard deviation from Eqs. (24) and (25).

We plot the error probability for individual detection with PC1 and PC2 in Figs. 7(a) and 7(b), respectively. We compare ideal photon counters with values of $K = 1, 2, 3$. For PC1 and both background scenarios of $N_B = 20$ and $N_B = 1000$, all variants clearly outperform the CS reference and for a resolution of $K \ge 2$, the resulting error coincides with the full-resolution counter. The associated low average photon number $N_1 \approx 0.11 \ll 1$ under both hypotheses and for both background scenarios explains why a binary SPD is close to being optimal. The reason why a higher resolution does not become more relevant in more noisy scenarios is that the optimal mixer gain, G^*,

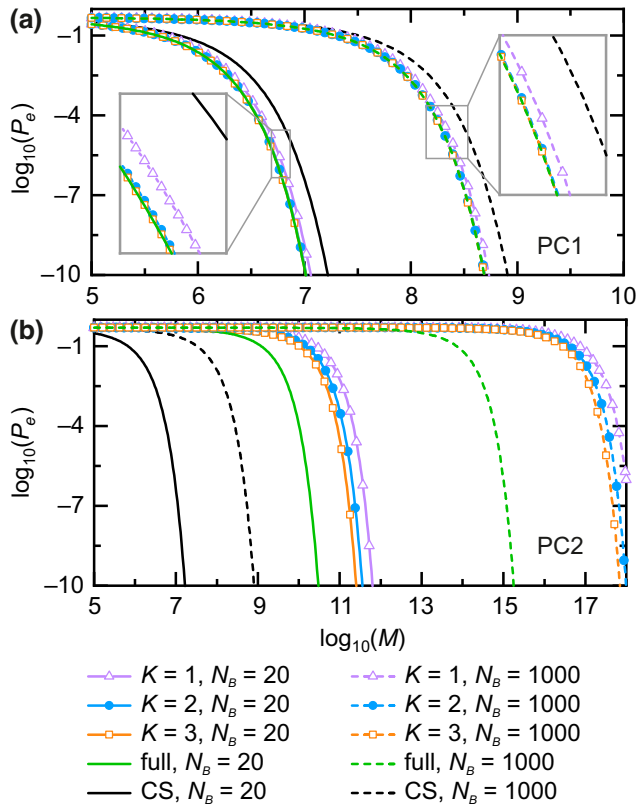

FIG. 7. The error probability P_e as a function of the number of transmitted modes M for different resolutions K for individual detection with (a) PC1 and (b) PC2. The solid lines show the performance for the low-noise regime, $N_B = 20$, and the dashed lines for the high-noise regime, $N_B = 1000$. The mean signal photon number is $N_S = 0.01$ and the reflectivity $\kappa = 0.01$ in both cases. The mixer gain is set to $G = G^*$.

decreases with increasing N_B, such that N_1 stays similar for varying N_B. This finding is important for real-world applications with a naturally high number of noise photons. Conversely, detection with PC2 alone is always inferior in comparison to the optimum classical scheme due to the large value of N_2, which is governed by strong background noise coupled to the return mode [cf. Eq. (14)].

IV. CONCLUSIONS

The experimental demonstration of a QA in quantum sensing protocols is a demanding task due to the stringent requirements on experimental imperfections. As a consequence, successful implementations in the optical regime, as well as at microwave carrier frequencies, have so far achieved a QA of only around 0.8 dB [10,19] out of the potentially obtainable 3 dB. Here, we have performed a detailed analysis of particular experimental imperfections on the QI performance for the PM-type receiver schemes. In this context, we have focused on the performance of single-photon counters, which represent one of the central elements of QI protocols. We have compared individual single-photon detection to correlated difference detection and found that the latter performs slightly better for different noise regimes. We have analyzed the role of respective weighting of the individual detector outcomes and identified the adjusted ratio for the optimal QI performance [cf. Eq. (21)]. While large $N_B \approx 1000$ theoretically gives access to a larger QA and matches realistic noise values at gigahertz frequencies, the detection unit needs to be able to handle corresponding return signal powers. Respectively, the mixer needs to operate at signal powers on the order of $N_B\hbar\omega$ without suffering from compression effects; the same applies to PC2 [cf. Eq. (14)]. As a consequence, currently available PCs with a photon-number resolution of up to three photons already yield a clearly deteriorated performance of PC2 for small $N_B \approx 10$, such that CPC does not seem to be suitable for near-term implementations. In contrast, individual detection with PC1 with limited photon-number resolution, $K \leq 3$, reaches a reasonable QA even for large $N_B \approx 1000$. As we have noted, the maximum achievable QA with PM-type receivers increases with increasing N_B and saturates at 3 dB for large N_B, which imposes further restrictions on low-N_B implementations [10]. Therefore, individual detection with PC1 for large N_B may be the simplest route toward the practical 3-dB QA with the currently available technology. Finally, our presented results also provide valuable insights into neighboring research fields, such as quantum communication [40–42]. While the fundamental hurdle of transmitting quantum signals at microwave frequencies over free-space channels remains an ongoing challenge, careful analysis of suitable operation scenarios represents a decisive step toward experimental realization.

ACKNOWLEDGMENTS

We acknowledge support by the German Research Foundation (Deutsche Forschungsgemeinschaft, DFG) via Germany's Excellence Strategy (Grant No. EXC-2111-390814868) and the German Federal Ministry of Education and Research (Bundesministerium für Bildung und Forschung, BMBF) via the QUARATE project (Grant No.13N15380). This research is part of the Munich Quantum Valley, which is supported by the Bavarian state government with funds from the Hightech Agenda Bayern Plus.

APPENDIX: COVARIANCES IN THE (UN)BALANCED DIFFERENCE DETECTION

The covariance between $\hat{N}_1$ and $\hat{N}_2$ is given by

$$\mathrm{Cov}\left(\hat{N}_1, \hat{N}_2\right) = \mathrm{Cov}\left(\hat{b}_1^\dagger \hat{b}_1, \hat{b}_2^\dagger \hat{b}_2\right) = \\ = \langle \hat{b}_1^\dagger \hat{b}_1 \hat{b}_2^\dagger \hat{b}_2 \rangle - \langle \hat{b}_1^\dagger \hat{b}_1 \rangle \langle \hat{b}_2^\dagger \hat{b}_2 \rangle. \quad \text{(A1)}$$

For a complex random vector $X = (X^1, \ldots, X^n)$, we introduce the moment notation

$$m^i = \langle X^i \rangle, \quad m^{ij} = \langle X^i X^j \rangle, \ldots \tag{A2}$$

The fourth-order moment can be expressed as

$$m^{ijkl} = c^{ijkl} + c^i c^{jkl}[4] + c^{ij} c^{kl}[3] + c^i c^j c^{kl}[6] + c^i c^j c^k c^l, \tag{A3}$$

where $c^i, \ldots, c^{ijkl}$ denote the cumulants of order 1–4 and the numbers in the square brackets indicate the number of terms contained in each expression as the indices rotate, i.e., $i \to j, j \to k$, etc. For Gaussian states, cumulants of order ≥ 3 vanish and the fourth-order moment simplifies to

$$m^{ijkl}_{\text{Gauss}} = c^{ij} c^{kl}[3] + c^i c^j c^{kl}[6] + c^i c^j c^k c^l. \tag{A4}$$

The remaining first- and second-order cumulants are connected to the moments via

$$c^i = m^i \quad \text{and} \quad c^{ij} = m^{ij} - m^i m^j. \tag{A5}$$

Since the first-order signal moments and the corresponding first-order cumulants vanish for $\hat{b}_1$ and $\hat{b}_2$, the fourth-order signal moment from Eq. (A1) simplifies to

$$\langle \hat{b}_1^\dagger \hat{b}_1 \hat{b}_2^\dagger \hat{b}_2 \rangle = \langle \hat{b}_1^\dagger \hat{b}_1 \rangle \langle \hat{b}_2^\dagger \hat{b}_2 \rangle + \langle \hat{b}_1^\dagger \hat{b}_2^\dagger \rangle \langle \hat{b}_1 \hat{b}_2 \rangle + \langle \hat{b}_1^\dagger \hat{b}_2 \rangle \langle \hat{b}_1 \hat{b}_2^\dagger \rangle, \tag{A6}$$

where we have used the expressions from Eq. (A5). The covariance between $\hat{N}_1$ and $\hat{N}_2$ reduces to

$$\text{Cov}\left(\hat{N}_1, \hat{N}_2\right) = \langle \hat{b}_1^\dagger \hat{b}_2^\dagger \rangle \langle \hat{b}_1 \hat{b}_2 \rangle + \langle \hat{b}_1^\dagger \hat{b}_2 \rangle \langle \hat{b}_1 \hat{b}_2^\dagger \rangle. \tag{A7}$$

The expressions from Eqs. (19) and (20) can be straightforwardly derived by the insertion of Eqs. (6), (7), and (11) into Eq. (A7).

[1] S. Lloyd, Enhanced sensitivity of photodetection via quantum illumination, Science **321**, 1463 (2008).

[2] S.-H. Tan, B. I. Erkmen, V. Giovannetti, S. Guha, S. Lloyd, L. Maccone, S. Pirandola, and J. H. Shapiro, Quantum illumination with Gaussian states, Phys. Rev. Lett. **101**, 253601 (2008).

[3] B. Kraus and J. I. Cirac, Discrete entanglement distribution with squeezed light, Phys. Rev. Lett. **92**, 013602 (2004).

[4] E. P. Menzel, R. Di Candia, F. Deppe, P. Eder, L. Zhong, M. Ihmig, M. Haeberlein, A. Baust, E. Hoffmann, D. Ballester, K. Inomata, T. Yamamoto, Y. Nakamura, E. Solano, A. Marx, and R. Gross, Path entanglement of continuous-variable quantum microwaves, Phys. Rev. Lett. **109**, 250502 (2012).

[5] S. Pogorzalek, K. G. Fedorov, M. Xu, A. Parra-Rodriguez, M. Sanz, M. Fischer, E. Xie, K. Inomata, Y. Nakamura, E. Solano, A. Marx, F. Deppe, and R. Gross, Secure quantum remote state preparation of squeezed microwave states, Nat. Commun. **10**, 2604 (2019).

[6] K. G. Fedorov, M. Renger, S. Pogorzalek, R. Di Candia, Q. Chen, Y. Nojiri, K. Inomata, Y. Nakamura, M. Partanen, A. Marx, R. Gross, and F. Deppe, Experimental quantum teleportation of propagating microwaves, Sci. Adv. **7**, eabk0891 (2021).

[7] Q. Zhuang, Z. Zhang, and J. H. Shapiro, Optimum mixed-state discrimination for noisy entanglement-enhanced sensing, Phys. Rev. Lett. **118**, 040801 (2017).

[8] H. Shi, B. Zhang, and Q. Zhuang, Fulfilling entanglement's optimal advantage via converting correlation to coherence, ArXiv:2207.06609, 1 (2022).

[9] S. Guha and B. I. Erkmen, Gaussian-state quantum-illumination receivers for target detection, Phys. Rev. A **80**, 052310 (2009).

[10] R. Assouly, R. Dassonneville, T. Peronnin, A. Bienfait, and B. Huard, Quantum advantage in microwave quantum radar, Nat. Phys. **19**, 1418 (2023).

[11] U. Las Heras, R. Di Candia, K. G. Fedorov, F. Deppe, M. Sanz, and E. Solano, Quantum illumination reveals phase-shift inducing cloaking, Sci. Rep. **7**, 9333 (2017).

[12] M. Reichert, Q. Zhuang, J. H. Shapiro, and R. Di Candia, Quantum illumination with a hetero-homodyne receiver and sequential detection, Phys. Rev. Appl. **20**, 014030 (2023).

[13] M. Sanz, U. Las Heras, J. J. García-Ripoll, E. Solano, and R. Di Candia, Quantum estimation methods for quantum illumination, Phys. Rev. Lett. **118**, 070803 (2017).

[14] W. Zhong, W.-Y. Zhu, Y. Li, L. Zhou, M.-M. Du, and Y.-B. Sheng, Relation between quantum illumination and quantum parameter estimation, ArXiv:2308.07150, 1 (2023).

[15] M. Renger, S. Pogorzalek, Q. Chen, Y. Nojiri, K. Inomata, Y. Nakamura, M. Partanen, A. Marx, R. Gross, F. Deppe, and K. G. Fedorov, Beyond the standard quantum limit for parametric amplification of broadband signals, npj Quantum Inf. **7**, 160 (2021).

[16] F. Kronowetter, F. Fesquet, M. Renger, K. Honasoge, Y. Nojiri, K. Inomata, Y. Nakamura, A. Marx, R. Gross, and K. G. Fedorov, Quantum microwave parametric interferometer, Phys. Rev. Appl. **20**, 024049 (2023).

[17] G. Sorelli, N. Treps, F. Grosshans, and F. Boust, Detecting a target with quantum entanglement, IEEE Aerosp. Electron. Syst. Mag. **37**, 68 (2022).

[18] S. Kay, *Fundamentals of Statistical Signal Processing: Detection Theory* (Prentice-Hall PTR, New Jersey (USA), 1998). https://books.google.de/books?id=vA9LAQAAIAAJ.

[19] Z. Zhang, S. Mouradian, F. N. C. Wong, and J. H. Shapiro, Entanglement-enhanced sensing in a lossy and noisy environment, Phys. Rev. Lett. **114**, 110506 (2015).

[20] G. Romero, J. J. Garcia-Ripoll, and E. Solano, Microwave photon detector in circuit QED, Phys. Rev. Lett. **102**, 173602 (2009).

[21] F. Helmer, M. Mariantoni, E. Solano, and F. Marquardt, Quantum nondemolition photon detection in circuit QED and the quantum Zeno effect, Phys. Rev. A **79**, 052115 (2009).

[22] K. Koshino, K. Inomata, T. Yamamoto, and Y. Nakamura, Implementation of an impedance-matched Λ system by dressed-state engineering, Phys. Rev. Lett. **111**, 153601 (2013).

[23] S. R. Sathyamoorthy, L. Tornberg, A. F. Kockum, B. Q. Baragiola, J. Combes, C. M. Wilson, T. M. Stace, and G. Johansson, Quantum nondemolition detection of a propagating microwave photon, Phys. Rev. Lett. **112**, 093601 (2014).

[24] B. Fan, G. Johansson, J. Combes, G. J. Milburn, and T. M. Stace, Nonabsorbing high-efficiency counter for itinerant microwave photons, Phys. Rev. B **90**, 035132 (2014).

[25] O. Kyriienko and A. S. Sorensen, Continuous-wave single-photon transistor based on a superconducting circuit, Phys. Rev. Lett. **117**, 140503 (2016).

[26] Sankar Raman Sathyamoorthy, Thomas M. Stace, and Göran Johansson, Detecting itinerant single microwave photons, C. R. Phys. **17**, 756 (2016).

[27] Xiu Gu, Anton Frisk Kockum, Adam Miranowicz, Yu-xi Liu, and Franco Nori, Microwave photonics with superconducting quantum circuits, Phys. Rep. **718–719**, 1 (2017).

[28] C. H. Wong and M. G. Vavilov, Quantum efficiency of a single microwave photon detector based on a semiconductor double quantum dot, Phys. Rev. A **95**, 012325 (2017).

[29] J. Leppäkangas, M. Marthaler, D. Hazra, S. Jebari, R. Albert, F. Blanchet, G. Johansson, and M. Hofheinz, Multiplying and detecting propagating microwave photons using inelastic Cooper-pair tunneling, Phys. Rev. A **97**, 013855 (2018).

[30] B. Royer, A. L. Grimsmo, A. Choquette-Poitevin, and A. Blais, Itinerant microwave photon detector, Phys. Rev. Lett. **120**, 203602 (2018).

[31] Y.-F. Chen, D. Hover, S. Sendelbach, L. Maurer, S. T. Merkel, E. J. Pritchett, F. K. Wilhelm, and R. McDermott, Microwave photon counter based on Josephson junctions, Phys. Rev. Lett. **107**, 217401 (2011).

[32] K. Inomata, Z. Lin, K. Koshino, W. D. Oliver, J.-S. Tsai, T. Yamamoto, and Y. Nakamura, Single microwave-photon detector using an artificial Λ-type three-level system, Nat. Commun. **7**, 12303 (2016).

[33] J.-C. Besse, S. Gasparinetti, M. C. Collodo, T. Walter, P. Kurpiers, M. Pechal, C. Eichler, and A. Wallraff, Single-shot quantum nondemolition detection of individual itinerant microwave photons, Phys. Rev. X **8**, 021003 (2018).

[34] S. Kono, K. Koshino, Y. Tabuchi, A. Noguchi, and Y. Nakamura, Quantum non-demolition detection of an itinerant microwave photon, Nat. Phys. **14**, 546 (2018).

[35] A. Narla, S. Shankar, M. Hatridge, Z. Leghtas, K. M. Sliwa, E. Zalys-Geller, S. O. Mundhada, W. Pfaff, L. Frunzio, R. J. Schoelkopf, and M. H. Devoret, Robust concurrent remote entanglement between two superconducting qubits, Phys. Rev. X **6**, 031036 (2016).

[36] R. Lescanne, S. Deléglise, E. Albertinale, U. Réglade, T. Capelle, E. Ivanov, T. Jacqmin, Z. Leghtas, and E. Flurin, Irreversible qubit-photon coupling for the detection of itinerant microwave photons, Phys. Rev. X **10**, 021038 (2020).

[37] R. Dassonneville, R. Assouly, T. Peronnin, P. Rouchon, and B. Huard, Number-resolved photocounter for propagating microwave mode, Phys. Rev. Appl. **14**, 044022 (2020).

[38] H. Yang, N. Samantaray, and J. Jeffers, Quantum illumination with multiplexed photodetection, Phys. Rev. Appl. **18**, 034021 (2022).

[39] L. Balembois, J. Travesedo, L. Pallegoix, A. May, E. Billaud, M. Villiers, D. Estève, D. Vion, P. Bertet, and E. Flurin, Practical single microwave photon counter with 10^{-22} $\mathrm{W}/\sqrt{\mathrm{Hz}}$ sensitivity, ArXiv:2307.03614, 1 (2023).

[40] S. Pirandola, Composable security for continuous variable quantum key distribution: Trust levels and practical key rates in wired and wireless networks, Phys. Rev. Res. **3**, 043014 (2021).

[41] M. Zhang, S. Pirandola, and K. Delfanazari, Millimetre-waves to terahertz SISO and MIMO continuous variable quantum key distribution, ArXiv:2301.04723, 1 (2023).

[42] F. Fesquet, F. Kronowetter, M. Renger, Q. Chen, K. Honasoge, O. Gargiulo, Y. Nojiri, A. Marx, F. Deppe, R. Gross, and K. G. Fedorov, Perspectives of microwave quantum key distribution in the open air, Phys. Rev. A **108**, 032607 (2023).